

THE INFLUENCE OF ORBITAL RESONANCES ON THE WATER TRANSPORT TO OBJECTS IN THE CIRCUMPRIMARY HABITABLE ZONE OF BINARY STAR SYSTEMS

DAVID BANCELIN,¹ ELKE PILAT-LOHINGER,¹ THOMAS I. MAINDL,¹ FLORIAN RAGOSSNIG,¹ AND CHRISTOPH SCHÄFER²

¹*Institut für Astrophysik
Universität Wien, Türkenschanzstr. 17*

A-1180 Vienna, Austria

²*Institut für Astronomie und Astrophysik
Eberhard Karls Universität Tübingen, Auf der Morgenstelle 10
D-72076 Tübingen, Germany*

(Received September 7, 2018; Revised XXX; Accepted XXX)

Submitted to ApJ

ABSTRACT

We investigate the role of secular and mean motion resonances on the water transport from a belt of icy asteroids onto planets or embryos orbiting inside the circumprimary habitable zone (HZ) of a binary star system. In addition, the host-star has an accompanying gas giant planet. For a comparison, we perform two case studies where a secular resonance (SR) is located either inside the HZ close to 1.0 au (causing eccentric motion of a planet or embryos therein) or in the asteroid belt, beyond the snow line. In the latter case, a higher flux of icy objects moving towards the HZ is expected. Collisions between asteroids and objects in the HZ are treated analytically. Our purely dynamical study shows that the SR in the HZ boosts the water transport; however, collisions can occur at very high impact speeds. In this paper, we treat for the first time, realistic collisions using a GPU 3D-SPH code to assess the water loss in the projectile. Including the water loss into the dynamical results, we get more realistic values for the water mass fraction of the asteroid during an impact. We highlight that collisions occurring at high velocities greatly reduce the water content of the projectile and thus the amount of water transported to planets or embryos orbiting inside the HZ. Moreover, we discuss other effects that could modify our results, namely the asteroid's surface rate recession due to ice sublimation and the atmospheric drag contribution on the asteroids' mass loss.

Keywords: celestial mechanics — minor planets, asteroids: general — binaries: general — methods: numerical — methods: analytical

1. INTRODUCTION

For studies of Earth analogs in planetary systems, the existence of water on such objects defines the habitability of this planet. The origin of water on Earth is still an open question and subject of debates leading to controversies. Endogenous and exogenous (asteroids, comets, and planetary embryos) were suggested separately to explain the water content of the Earth. It was believed that the water presently on Earth was carried by comets from the Oort cloud in the late veneer scenario (Owen and Bar-Nun 1995) or from the Jupiter family. However, both astronomical and geochemical analyses (Lécuyer et al. 1998) and the recent data from Rosetta (Altwegg et al. 2015) showed heterogeneous distributions of the D/H ratio compared to the Earth’s. Since, models advocating impacts of large number of asteroids are favored.

It is well known that orbital resonances – i.e. mean motion (MMR) and secular resonances (SR) – play a key role in the architecture of a planetary system as shown in various studies for our solar system (Tsiganis et al. 2005; Gomes et al. 2005; Walsh et al. 2011) and in binary systems (Mudryk and Wu 2006; Thebault and Haghighipour 2014). Icy bodies trapped in orbital resonances are also potential water sources for objects orbiting inside the habitable zone (HZ). These water-rich bodies are either planetary embryos (Haghighipour and Raymond 2007) or asteroids as shown for our Earth in Morbidelli et al. (2000) and O’Brien et al. (2014). More recently, Bancelin et al. (2015) gave a statistical estimate of the contribution of asteroids in bearing water material onto the circumprimary HZ of binary star systems. They showed that the differences in the statistical results strongly depend on the initial configuration of the binary star systems hosting a gas giant. Bancelin et al. (2016) showed that in such configurations an SR can be located within the planetesimal belt where an overlap with MMRs may lead to strong perturbations causing a flux of asteroids moving towards the HZ. In the case of icy asteroids, they will contribute to the water transport onto a planet moving in the HZ. Studies by Pilat-Lohinger et al. (2016) and Bazzó et al. (2017) introduced a quick semi-analytical method to determine the location of the linear SR. This method showed clearly how the position of the SR depends on the semi-major axis, the eccentricity and the mass of both the giant planet and the secondary star. Thus, in certain binary-planet configurations, the SR may help to transport water into the HZ. While in other cases the highly eccentric motion due to the SR may influence the habitability of a planetary system as it was shown for the solar system by Pilat-Lohinger et al. (2008a), Pilat-Lohinger et al. (2008b) and Pilat-Lohinger (2015).

The aim of the present study is, on one hand, to highlight in detail the influence of orbital resonances on the water transport by icy asteroids from a planetesimal belt to bigger

objects (embryos or planets) orbiting the host-star within the HZ. On the other hand, most studies of planetary formation performed so far do not treat collisions properly. Indeed, collisions occur far from the real collision distance (generally at several Hill radii) and using a perfect merging approach. This in turn can result in overestimating the size and the water content of the body resulting from this collision. In this paper, we also aim to provide, for the first time, a comparison between a purely merging approach and more realistic collisions using a GPU 3D-SPH code to model the water transferred from a small projectile (asteroid) to a bigger target (Moon-, Mars-, and Earth-sized objects).

For various binary star-giant planet configurations, we investigate the two following scenarios.

- (1) Eccentric planetary motion inside the HZ (induced by an SR at ~ 1.0 au and/or MMRs) and an asteroid belt perturbed by MMRs.
- (2) Nearly circular planetary orbits inside the HZ and an asteroid belt perturbed by an SR and MMRs.

In Sect. 2, we define our dynamical model for the various binary star systems, the gas giant and an icy asteroid belt. We also describe therein our algorithm for the collision assessment. The results are presented and analyzed in Sect. 3. Finally, we discuss in Sect. 4 the possibility of processes causing water loss from an asteroid’s surface, e.g. ice sublimation and atmospheric pressure.

2. METHODS

2.1. Binary stars and gas giant configurations

We focused our work on binary star systems with two G-type stars with mass equal to $1M_{\odot}$. The initial orbital separations are $a_b = 50$ au or 100 au and the binary’s eccentricity is $e_b = 0.1$ or 0.3. Since we study the planar case, all initial inclinations are set to 0° . Our studied systems host a gas giant planet initially moving on a circular orbit with a mass equal to the mass of Jupiter. As pointed out by Pilat-Lohinger et al. (2016), the location of the SR depends both on the orbital elements of the secondary and the gas giant. Since we fixed the binary’s semi-major axis to 50 and 100 au for our numerical study, the position of the gas giant (a_{GG}) changes for the different systems depending on whether we analyze the perturbation of the SR in the HZ or how the SR affects the water transport. The latter can be considered as a positive influence on the habitability because the SR is located in the planetesimal belt, which is beyond 2.7 au. With the conditions that the SR should either be beyond 2.7 au or around 1.0 au, we determine the according semi-major axis of the giant planet using the semi-analytical method of Pilat-Lohinger et al. (2016) and Bazzó et al. (2017). We summarize the values of a_{GG} in Tab. 1.

Table 1. Gas giant’s semi-major axis a_{GG} according to the binary’s periapsis distance q_b . Second and third columns are values of a_{GG} such as the secular resonance (SR) lies inside the HZ or inside the asteroid belt, respectively.

q_b (au)	a_{GG} (au) (SR inside HZ)	a_{GG} (au) (SR inside the disk)
35	3.00	5.2
45	3.10	5.2
70	4.75	7.2
90	4.5	7.2

2.2. Icy Planetesimals Disk Modeling

We modeled a disk of 1000 icy Ceres-like planetesimals with mass $M_{CERES} = 4.76 \times 10^{-10} M_{\odot}$ inside and beyond the orbit of the gas giant. They have initially nearly circular and planar orbits with initial eccentricities and inclinations randomly chosen below 0.01 and 1° , respectively. To avoid strong initial interactions with the gas giant, we assumed that it has gravitationally cleared a path in the disk around its orbit. We defined the width of this path as $\pm 3R_{H,GG}$, where $R_{H,GG}$ is the giant planet’s Hill radius. The small bodies’ semi-major axis a_A is uniformly distributed into three regions from an inner to an outer border, the latter being defined by the stability criteria (Holman and Wiegert 1999; Pilat-Lohinger and Dvorak 2002). The three regions are defined as follows.

1. \mathcal{R}_1 is for $2.0 \leq a_A \leq 2.7$ au,
2. \mathcal{R}_2 is for $2.7 \leq a_A \leq a_{GG} - 3R_{H,GG}$,
3. \mathcal{R}_3 is for $a_A \geq a_{GG} + 3R_{H,GG}$

Because of this definition, region \mathcal{R}_2 does not exist for the binary with $q_b = 35$ au and 45 au as $a_{GG} - 3R_{H,GG} < 2.7$ au.

Each asteroid is assigned a water mass fraction (hereafter wmf) using a linear approximation and with borders defined in the following way.

1. $a_A \in \mathcal{R}_1$, $1 \leq \text{wmf} \leq 10\%$
2. $a_A \in \mathcal{R}_2$, $10 \leq \text{wmf} \leq 15\%$
3. $a_A \in \mathcal{R}_3$, $\text{wmf} = 20\%$

Because the distribution of a_A within the disk is different for the various binaries investigated (as it depends on the location of the gas giant) the total amount of water \mathcal{W}_{TOT} (expressed in Earth-ocean unit¹) contained in the disk also varies, as shown in Tab. 2.

¹ one Earth-ocean weights 1.5×10^{21} kg of H₂O

Table 2. Total amount of water \mathcal{W}_{TOT} (expressed in Earth-ocean unit) contained in the icy asteroids belt.

q_b (au)	\mathcal{W}_{TOT} (Earth-ocean) (SR inside HZ)	\mathcal{W}_{TOT} (Earth-ocean) (SR inside the disk)
35	58.6	78.2
45	60.2	78.2
70	75.6	81.5
90	76.7	81.5

2.3. Impact modeling

The minimum orbital intersection distance (MOID) is widely used in celestial mechanics to determine whether an object can be a potential danger for the Earth. The MOID corresponds to the closest distance between two keplerian orbits, regardless their real position on their respective trajectories. For our study, we need to derive the MOID in order to simulate impacts between icy objects initially located in the asteroid belt and embryos-to-planet-sized bodies (EPs) initially inside the HZ. They are either Moon- and Mars-sized (embryos) or Earth-sized (planets) (see Table 3 for the physical mass and radius). For this purpose, we performed for both scenarios (i.e. the SR either inside the HZ or inside the asteroid belt) two separate simulations: considering the gravitational perturbations of the stars and the gas giant, we integrated separately for 100 Myr using the Radau integrator.

- (1) The asteroid belt to assess the orbital distribution of asteroids reaching distances $r_A < 2.0$ au to the primary star. Figure 1 shows the cumulative distribution of the number of crossings as a function of r_A au for the different binary star systems investigated and for several integration times. The left panels show results for a SR lying inside the HZ and the right panels are the results for the SR in the asteroid belt. As indicated by the different colors, one can see that in both cases, asteroids can rapidly increase their eccentricity and reach Mercury’s distances within 1 Myr (blue histograms). We can also notice that the number of crossings is higher when the SR is located inside the belt (right panels). This was also pointed out by Bancelin et al. (2016) and can be explained by possible overlaps of the SR with MMRs.
- (2) EPs at initial location a_{EP} to assess the evolution of their eccentricity with time. They are uniformly distributed over 48 positions within the HZ (with borders defined according to Kopparapu et al. (2013)) and initially move in circular orbits.

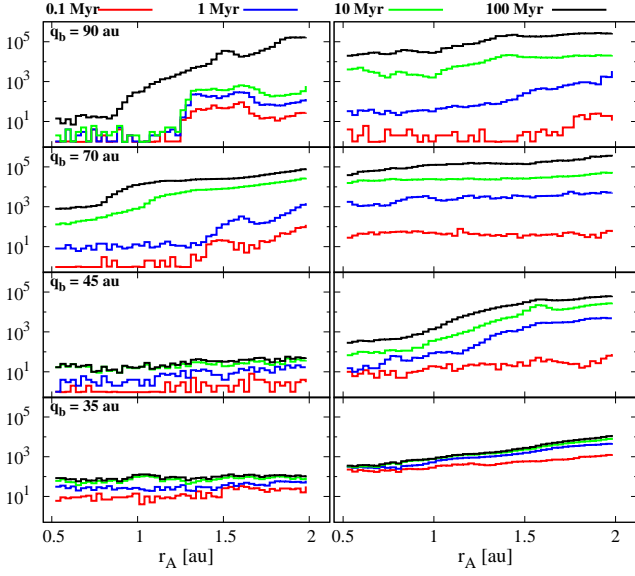


Figure 1. Cumulative distribution of r_A for asteroids reaching distances < 2.0 au. The color lines indicate different integration times. The panels show the results for the studied q_b (increasing q_b from bottom to top). Left and right panels are for the SR lying inside or outside the HZ, respectively.

Table 3. Physical parameters, mass M_{EP} and radius R_{EP} , of the EPs considered in our simulations expressed in Earth-mass ($M_{\oplus} = 3.0 \times 10^{-6} M_{\odot}$) and Earth-radius ($R_{\oplus} = 6378.0$ km)

	Mass M_{EP}	Radius R_{EP}
	(M_{\oplus})	(R_{\oplus})
Earth	1.000	1.00
Mars	0.100	0.53
Moon	0.012	0.27

We combined the results of these two integrations to analytically compute the MOID using the algorithm described in Sitarski (1968). We define a collision if the MOID is comparable to the EP's radius R_{EP} . For the collision assessment, we use the following five-steps algorithm.

- (1) For a given position a_{EP} , we check if $q_{EP} \leq r_A \leq Q_{EP}$ where q_{EP} and Q_{EP} are the periastris and apoapsis distances of the EPs respectively which are defined according to $e_{EP} = e_{\max}(t)$ with $e_{\max}(t)$ the maximum of the EP's eccentricity for different period of integration. If this condition is fulfilled, then we go to the next step.
- (2) In reality, e_{EP} has periodic variations between 0 (its initial value) and $e_{\max}(t)$. Thus, we define the function $Y(e_{EP}) = d_{\min}(e_{EP}) - R_{EP}$ where d_{\min} is the MOID. According to the sign of the product $Y(e_{EP} = 0) \times$

$Y(e_{EP} = e_{\max})$ we use different procedures: if the sign is negative then we use a regula falsi procedure in order to find the value of e_{EP} giving $Y(e_{EP}) \approx 0$. If the sign is positive, then we use a dichotomy procedure to find a value of e_{EP} leading to an impact.

- (3) When a collision is found, i.e. if $d_{\min} \leq R_{EP}$ we also derive, from the MOID, the true anomalies of the EP and the asteroid in order to compute the relative impact velocity and impact angle of the asteroid.
- (4) If the previous condition is fulfilled, then we define:

$$\begin{cases} \mathcal{W}_k(a_{EP}, t) = \frac{M_{\text{CERES}} \times wmf_k}{M_{\text{H}_2\text{O}}} \\ \widetilde{\mathcal{W}}_k(a_{EP}, t) = \frac{1}{N_k} \sum_{k=1}^{N_k} \frac{M_{\text{CERES}} \times wmf_k \times (1 - \omega_c(a_{EP}))}{M_{\text{H}_2\text{O}}} \end{cases}$$

as the quantity of water (in Earth-ocean unit) delivered by an asteroid number k (with water mass fraction wmf_k), at an intermediate integration time t , to the EP initially at a semi-major axis a_{EP} . Here, $M_{\text{H}_2\text{O}} = 1.5 \times 10^{21}$ kg of H_2O is the mass of one Earth-ocean. The first term \mathcal{W}_k assumes a merging approach in which the whole water content of the asteroid is delivered to the EP without assuming any water loss processes. The second term $\widetilde{\mathcal{W}}_k$ takes into account a water loss factor ω_c induced by a water loss mechanism. Here, N_k is the number of possible collisions of the asteroid k .

- (5) At the end of the procedure, we can derive the total fraction of water delivered to the EP: $\mathcal{W}_{EP}(a_{EP}, t) = \frac{1}{\mathcal{W}_{\text{TOT}}} \sum_{k=1}^{n_i} \mathcal{W}_k(a_{EP}, t)$ and $\widetilde{\mathcal{W}}_{EP}(a_{EP}, t) = \frac{1}{\widetilde{\mathcal{W}}_{\text{TOT}}} \sum_{k=1}^{n_i} \widetilde{\mathcal{W}}_k(a_{EP}, t)$ where n_i is the number of impactors. We also compute the median values of the asteroids' impact velocities $\bar{v}_i(a_{EP})$ and angles $\bar{\theta}_i(a_{EP})$ according to the total number of possible collisions found.

3. RESULTS

In Fig. 2, we show detailed results obtained when a SR is inside the HZ for a secondary either at $a_b = 50$ au (left panels) or at $a_b = 100$ au (right panels). For each binary's periastris distance we show the outcome for an Earth- (left sub-panels) and Mars/Moon-sized bodies (right sub-panels) as a function of their initial semi-major axis. From bottom to top, the panels represent in (a) the cumulative fraction of incoming water $\mathcal{W}_{EP}(a_{EP}, t)$ on the EP (for intermediate integration times $t = 0.1 - 1 - 10 - 100$ Myr in red, blue, green and solid black lines

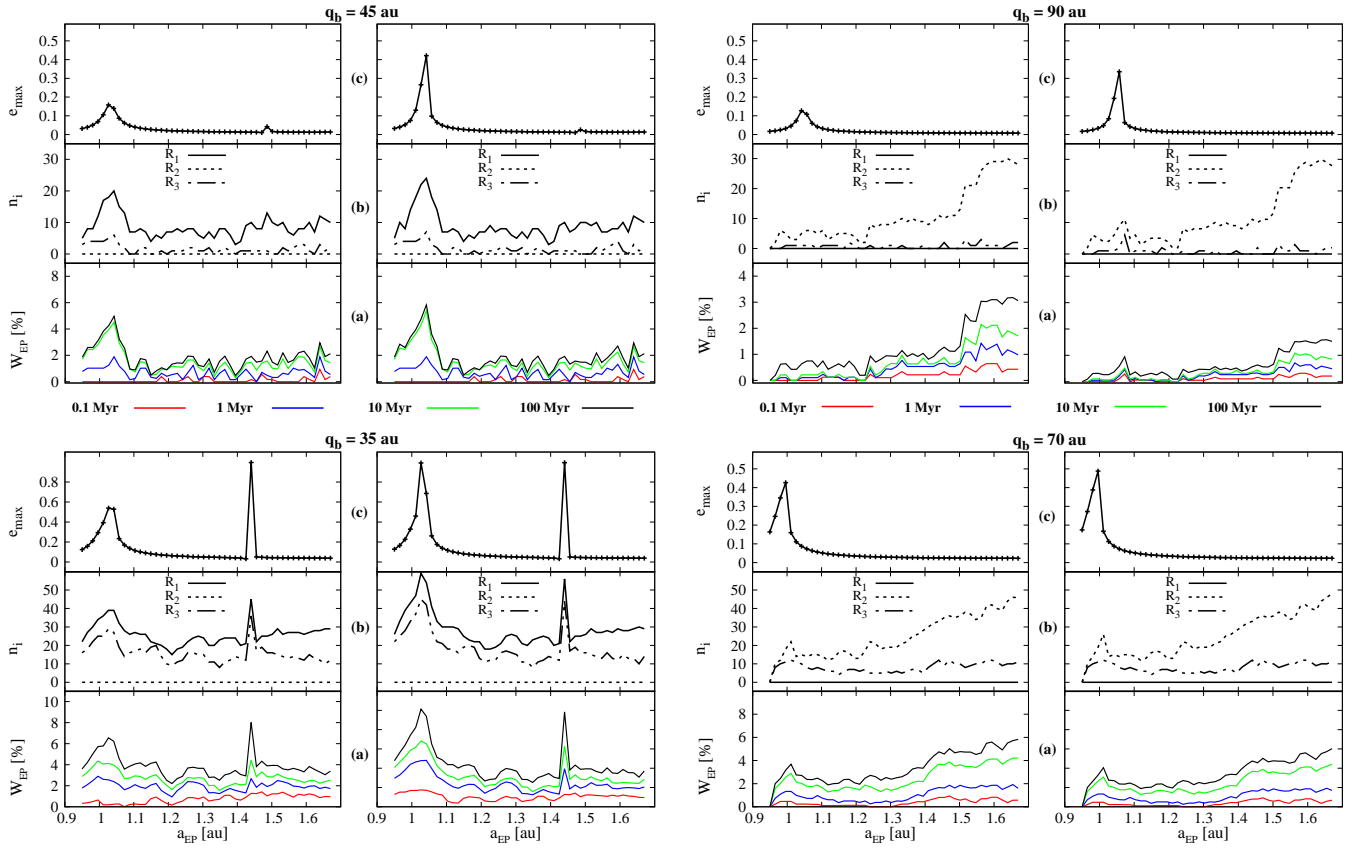


Figure 2. *Left and right panels:* results for $a_b = 50$ au and 100 au respectively. For a given value of q_b , the *left and right sub-panels* show results for an Earth- and Mars/Moon-like objects respectively. For each object, from bottom to top, are shown in (a) the fraction of incoming water \mathcal{W}_{EP} at the EP's surface for several timescales (0,1 Myr in red, 1 Myr in blue, 10 Myr in green and 100 Myr in black); in (b) the total number of impactors n_i (up to 100 Myr) for each initial region \mathcal{R}_1 (solid line), \mathcal{R}_2 (dashed line) and \mathcal{R}_3 (dotted-solid line); in (c) the maximum eccentricity e_{max} (up to 100 Myr).

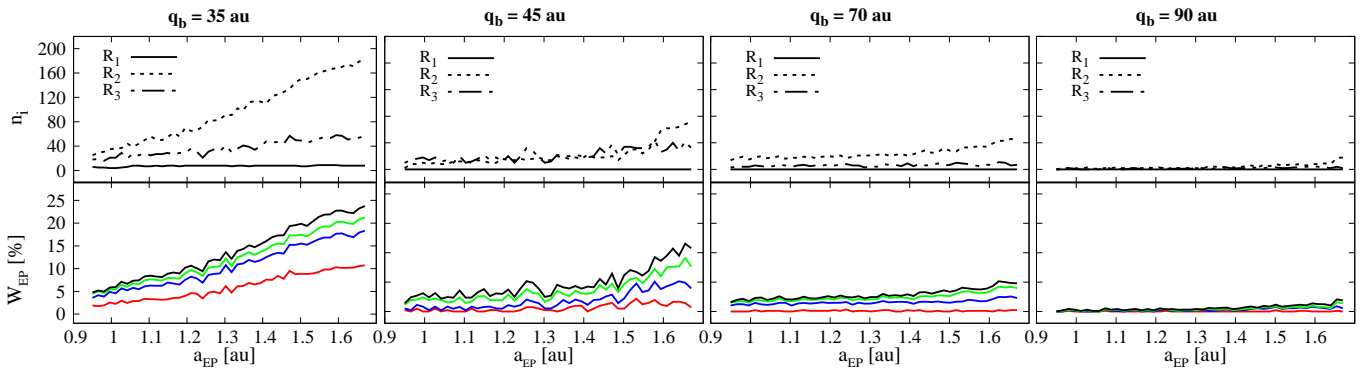


Figure 3. Same as in Fig. 2 but for the case of an SR inside the asteroid belt. From *left to right panels* are shown results for increasing value of q_b . As the eccentricity evolution is the same for each EP, only one of the EP's results is displayed for \mathcal{W}_{EP} (*bottom panel*) and n_i (*top panel*).

respectively); (b) the number of asteroids n_i impacting the EP's surface (at $t = 100$ Myr); (c) the maximum eccentricity e_{\max} reached by an EP (over $t = 100$ Myr). Similar results are presented in Fig. 3 for the case of a SR inside the asteroid belt. We did not represent the EP's eccentricity distribution in the HZ like in Fig. 1 because their orbit remains almost circular during the integration time, whatever the size of the EP. Besides, only results for one of the EPs are displayed.

3.1. Water transport: merging approach

In Fig. 2, one can recognize in sub-panels (c) the SR around 1.0 au causing a relatively high eccentric motion with decreasing q_b and M_{EP} . Due to the proximity of the gas giant, we can also notice, for $q_b = 35$ au, the presence of the 3:1 MMR at 1.44 au also causing high eccentric motions in this area. As a consequence, we can see for $a_b = 50$ au (left panels and sub-panels (b)) that an EP initially moving inside an orbital resonance can collide with more asteroids than if they were orbiting outside the SR or MMR. Both regions \mathcal{R}_1 and \mathcal{R}_3 can be water sources for EPs within the entire HZ. Indeed, as shown in the sub-panels (a), within the first 1 Myr, the quantity of water \mathcal{W}_{EP} delivered to an EP, initially located inside an orbital resonance, is boosted as it can encounter more asteroids, not only those crossing the HZ but also those with distance r_A beyond the HZ (see Fig. 1). For $a_b = 100$ au (right panels), despite the relatively high eccentricity of EPs around 1.0 au, n_i is mainly maximum for a_{EP} close to the outer border of the HZ, following the r_A distribution (see Fig. 1). Therefore, as shown in sub-panels (a), EPs at 1.0 au can attract equal or even less water than EPs outside the SR. For both values of a_b investigated, we can notice that n_i represents only a small fraction of the total number of asteroids in the disk (less than 10%). Also, \mathcal{W}_{EP} can reach a maximum of 9% of the total amount of water in the disk.

Figure 3 illustrates results for the second case (SR inside the belt). Because of the huge number of impactors, up to four times higher ($\sim 25\%$ of the initial population for instance for $q_b = 35$ au) than if a SR was inside the HZ, the water transport to the HZ is boosted and $\mathcal{W}_{\text{EP}} \sim 15\%$ for $q_b = 45$ au and even $\sim 25\%$ for $q_b = 35$ au. For each binary configuration studied, the main source of impactors is located in the region \mathcal{R}_2 . As already proved by Bancelin et al. (2016), this region is the primary source of icy asteroids reaching the HZ for this configuration, as both orbital resonances overlap in the asteroid belt. Contrary to the previous case (SR \in HZ), the water distribution in the HZ follows the r_A distribution and EPs located around 1.0 au, on circular motion, can interact with fewer icy asteroids than EPs located at larger semi major axes. Therefore, only a small fraction of the \mathcal{W}_{TOT} , less than 5%, can be transported to an EP.

3.2. Impact parameters statistics

In Fig. 4, we represent the impact angles and velocities distribution $\bar{\theta}_i$ and \bar{v}_i (top and bottom panels respectively). Results are compared for both locations of the SR: inside the HZ (grey solid line for $\bar{\theta}_i$ and panels (a) for \bar{v}_i) and outside the HZ (black solid line for $\bar{\theta}_i$ and panels (b) for \bar{v}_i). In the bottom panels, we distinguished impact velocities on Earth-, Mars- and Moon-sized objects (solid blue, red and black lines respectively). For both cases (SR inside and outside the HZ), the impact velocity distribution inside the HZ shows different modes depending on a_{EP} : outside the orbital resonances, statistically, we have for asteroids impacting an Earth-sized $1.0 < \bar{v}_i < 1.5 v_e$, a Mars-sized $1.5 < \bar{v}_i < 2.5 v_e$ and a Moon-sized $2.5 < \bar{v}_i < 6.0 v_e$ (all expressed in escape velocity v_e units of the respective EP). However, near an orbital resonance, \bar{v}_i can be slightly higher as seen in Fig. 4. For instance, for $q_b = 35$ au (for this particular system, one should read results for the Earth case on the left y-axis and for the Mars/Moon case on the right y-axis), \bar{v}_i can reach up to $6.0 v_e$ for objects impacting an Earth-, $25 v_e$ for a Mars- and beyond $40 v_e$ for a Moon-sized body. In a similar way, $\bar{\theta}_i$ has high variations between 20° and 80° mainly near the SR. However, when an EP is not initially located inside an orbital resonance (both Fig. 2 and 3), $\bar{\theta}_i$ is in average above 50° .

3.3. Real collision modeling and water loss

A key parameter of water and mass loss is the collision modeling itself when the asteroid arrives at the EP's surface. To verify the validity of the perfect merging assumption regarding collisional water loss, we performed simulations of water-rich Ceres-sized asteroids with dry targets in the mass range M_{EP} equal to $1 M_{\text{MOON}}$, $1 M_{\text{MARS}}$ and $1 M_{\text{EARTH}}$. We assume the Ceres-like impactor with $wmf = 15\%$ water content in a mantle around a rocky core. The simulations are performed with our parallel (GPU) 3D smooth particle hydrodynamics (SPH) code introduced by Maindl et al. (2013) and Schäfer et al. (2016). It includes self-gravity and implements solid-body continuum mechanics with a damage model for fracture and brittle failure along the lines of Benz and Asphaug (1994, 1995). The material behavior is modeled using the Tillotson equation of state (Tillotson 1962). A tensorial correction (Schäfer et al. 2007) warrants zeroth order consistency.

As we want to focus on merging, especially to verify a perfect merging assumption, we chose a collision angle leading to a merging outcome. Because larger angles result in hit-and-run configurations (Leinhardt and Stewart 2012; Maindl et al. 2014), we chose a smaller angle in order to ensure a merging configuration. We simulated impacts on targets with different sizes at an impact angle of 30° with initial collision velocities (taken from Fig. 4) $\bar{v}_i = 2; 5$ and $30 v_e$ for the Moon, $\bar{v}_i = 1; 5$ and $20 v_e$ for Mars and $\bar{v}_i = 1; 3$ and

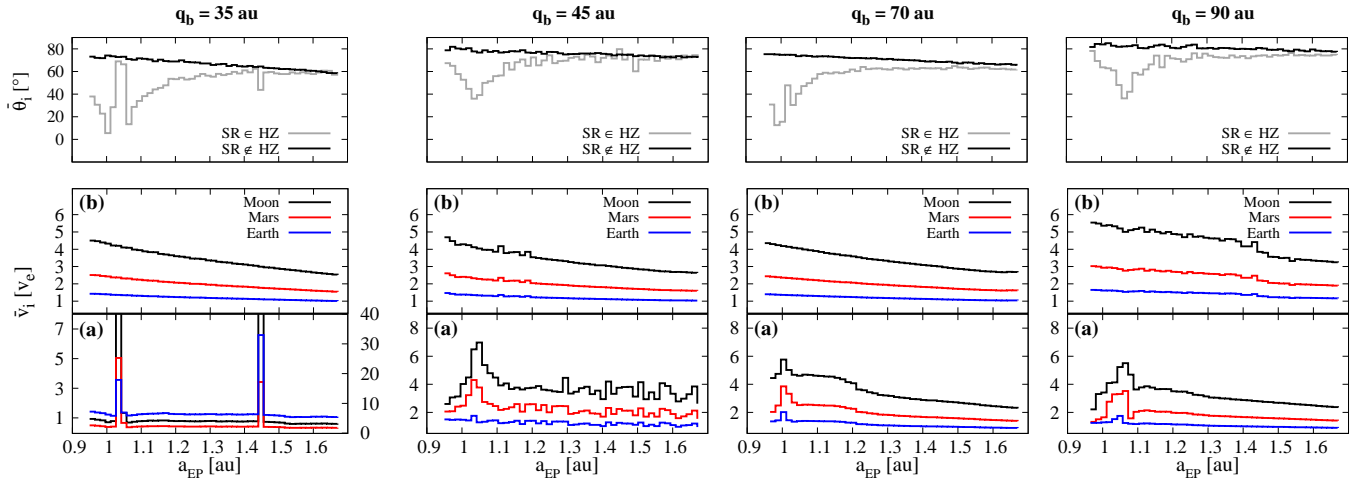


Figure 4. Impact angles $\bar{\theta}_i$ velocities \bar{v}_i (*top* and *bottom* panels respectively) with respect to a_{EP} and for increasing values of q_b from left to right. Colors in the *bottom* panels are for impact velocities at the surface of Earth, Mars and Moon objects (solid blue, red and black lines respectively) depending on whether SR lies inside or outside the HZ (panels *a* and *b* respectively). For $q_b = 35$ au, values of \bar{v}_i for Moon/Mars have to be read on the right y-axis as the values are much larger than the Earth (left y-axis). Colors in the *top* panel are for SR inside the HZ (solid grey line) or inside the belt (solid black line).

$5 v_e$ for the Earth. Except for this latter case ($\bar{v}_i = 5 v_e$) for which about 1 million SPH particles are used, most of the scenarios are resolved in about 500,000 SPH particles. All objects were relaxed by initializing them with self-consistent hydrostatic structures, and internal energies following adiabatic compression as described in [Burger \(2015\)](#).

In order to estimate an upper limit for water retained on the surviving body after the collision, we investigate the dynamics of matter ejected from the impact site². Collision fragments moving faster than the escape velocity are considered lost. This approach does not take into account losses due to (a) sublimation depending on the radiative environment of the individual collision and/or heating due to the impact process itself or (b) due to the interaction with an atmosphere that may survive the impact; we will model both aspects in a subsequent study. The water loss results therefore represent a lower loss limit. Figure 5 summarizes the water loss ω_c in the collision scenarios. All but the most extreme scenario result in a merged main survivor retaining most of the mass. The exception is the $30 v_e$ impact of a Ceres-like body onto the Moon which leads to mutual destruction of the bodies into a debris cloud and hence a loss of all volatile constituents. The other very fast impact (Mars at $20 v_e$) results in a merged survivor that retains just under 2 wt-% of the available water. For the lower collision velocities we observe water loss rates between 11 wt-% and 68 wt-%. This demonstrates that even with an approximate model, there are significantly different results compared to the perfect merging assumption. If plotted versus the impact velocity in terms of the mutual escape

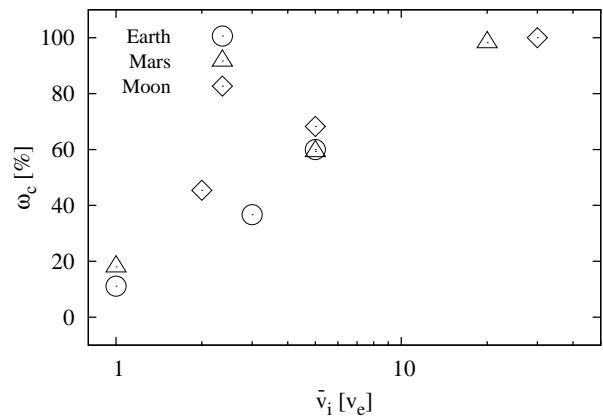


Figure 5. Water loss ω_c as a mass fraction of the initial total water after impacts at velocity \bar{v}_i in units of the EP's escape velocity v_e .

velocity as in Fig. 5, there is a strong correlation with the impact velocity but only weak dependence on the absolute mass.

3.4. Water transport due to real collisions

For a more realistic estimation of \mathcal{W}_{EP} , we use the previous results shown in Fig. 2 and 3 and take into account the fraction of water loss ω_c due to the physical impact between the asteroid and the EP of Fig. 5. Using a linear extrapolation of ω_c between the minimum and maximum impact velocities derived for each EP, we are able to provide better estimates for the water transport. In Fig. 6, we compare the fraction of water reaching the EP's surface with and without taking into account our study of SPH collisions represented by the solid

² Note that we use the term *ejecta* for material accelerated away from the impact site regardless whether it originates from the projectile or the target.

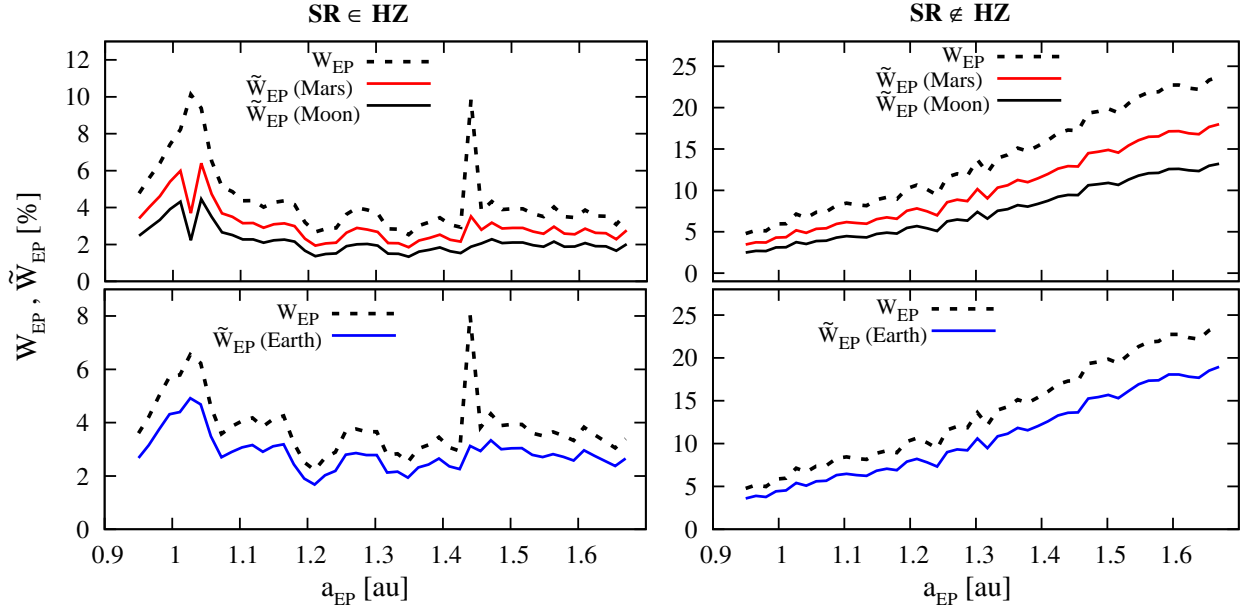


Figure 6. Fraction of incoming water with (solid lines) and without (dotted lines) our SPH collision model. *Left and right* panels are for SR inside the HZ and inside the asteroid belt, respectively.

and dotted lines respectively, i.e. $\tilde{\mathcal{W}}_{\text{EP}}$ and \mathcal{W}_{EP} . The two top panels show results for Moon- and Mars-sized objects and the bottom panels, for Earth-sized bodies. We show the comparison for a binary with $q_b = 35$ au and a computation of 100 Myr.

One can clearly see that collisions between EPs and asteroids are greatly overestimated if we consider a merging approach. Indeed, we highlight that close to the MMR inside the HZ, the water transport to an EP’s surface i.e. \mathcal{W}_{EP} can be reduced significantly by almost 50% for an Earth-, 68% for a Mars- and 75% for a Moon-sized object. We have the same statistics near the SR for a Mars- and Moon-sized except for an Earth as $\bar{v}_i = 3 v_e$. In this case, \mathcal{W}_{EP} is reduced by $\sim 30\%$. Even if no strong perturbation is located in the HZ (right panels), the real collision process shows that the incoming amount of water is reduced to $\tilde{\mathcal{W}}_{\text{EP}} \sim 50\% \mathcal{W}_{\text{EP}}$ for a Moon-sized EP and to $\sim 20\% \mathcal{W}_{\text{EP}}$ for a Mars- and Earth-sized body (right panels). A comparison of the left and respective right panels shows that around 1.0 au, $\tilde{\mathcal{W}}_{\text{EP}}$ is nearly the same in both cases (SR \in HZ and SR \notin HZ) which indicates the importance of including SPH collisions into dynamical studies to avoid false effects as shown by the dotted lines of the left panels in Fig. 6.

1. The apparent positive aspect of orbital resonances is that due to eccentric motion of the EP at 1.0 au, the transported water (\mathcal{W}_{EP}) is boosted and ensures higher values than in case of circular motion of the EP. Moreover, if SR \notin HZ, then even with a higher crossing frequency (see Fig. 1), the nearly circular motion of EPs

close to 1.0 au limits the number of collisions with asteroids.

2. On the other hand, the negative aspect of high eccentric motion near 1.0 au is the high impact velocities which drastically reduces the efficiency of the water transport and leading to significantly lower values of $\tilde{\mathcal{W}}_{\text{EP}}$. It seems that nearly circular motion in the HZ is important to prevent relatively high water loss during collision as \bar{v}_i are much lower when SR \notin HZ.

4. DISCUSSION: OTHER WATER LOSS PROCESSES

In this section, we discuss several processes that can significantly reduce the water content on the surface of an asteroid such as ice sublimation and atmospheric drag.

4.1. Ice sublimation

Recently, the Rosetta mission revealed that comet 67P/CG sublimated $3.5 \pm 0.5 \times 10^{28}$ H₂O molec/s after perihelion passage, implying a surface loss of 2–4 m (Hansen et al. 2016). Water sublimation also occurs on the surface of asteroids, even in the main-belt, as shown by Jewitt (2012). We used the same approach as Jewitt (2012) in order to estimate the surface recession rate of an asteroid due to ice sublimation by solving the following equation:

$$\frac{F_{\odot}(1-A)}{d_A^2 [\text{au}]} \cos \theta = \epsilon \sigma T^4 + L(T) \rho_{\text{ice}} \frac{dS}{dt}(T)$$

where

1. $F_{\odot} \sim 1360 \text{ W.m}^{-2}$ is the solar constant;

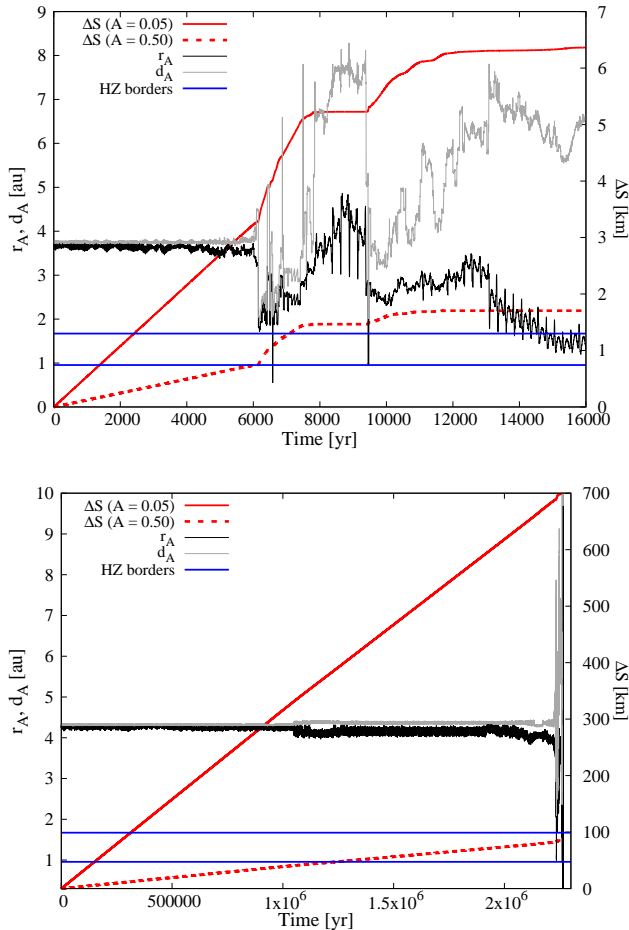


Figure 7. Evolution of the cumulative surface recession ΔS for an albedo $A = 0.05$ and $A = 0.50$ (solid and dashed lines, respectively). The heliocentric and mean distances r_A and d_A are represented (black and grey lines, resp.) together with the HZ borders (blue lines). Upper and bottom panels are for two asteroids with different orbital evolutions.

2. A , the bound albedo, is the product of the geometric albedo and the phase integral and defines the fraction of the total incident stellar radiation reflected by an object back to space. Asteroids can have $A \approx 0.5$, but most of them have a relatively low albedo (Shestopalov and Golubeva 2011). Ice material is known to be a good radiation reflector but the sublimation process is more efficient when the ice is dirty ($A = 0.05$) than clean ($A = 0.50$). In our simulations, we considered both values for comparison;
3. $d_A = \frac{q_A + Q_A}{2}$ is the mean distance to the primary star expressed in astronomical units and corresponds to the average distance value between the asteroid's periaapsis and apoapsis distance, q_A and Q_A respectively. We chose this definition in order to take into account the

non-circular motion of the asteroid. Indeed, using r_A would greatly overestimate the surface temperature of the asteroid in the case of an eccentric orbit, when integrating with time;

4. θ is the angle between the Sun-direction and the normal of a patch of the asteroid's surface. The surface temperature of the asteroid is minimized (assuming an isothermal surface) when $\cos\theta = 1/4$ and maximized (reached at the sub-solar point on a non-rotating body) when $\cos\theta = 1$. In our simulation, we consider only the sub-solar case as the isothermal case is negligible for main-belt asteroids;
5. ϵ is the emissivity of the surface, $\epsilon \sim 0.9$;
6. $\sigma = 5.67 \times 10^{-8} \text{ W.m}^{-2}.\text{K}^{-4}$ is the Boltzmann constant;
7. T is the equilibrium temperature at the surface expressed in K;
8. L is the latent heat of sublimation in J.kg^{-1} ;
9. $\rho_{ice} = 1000 \text{ kg.m}^{-3}$ is the ice density;
10. $\frac{dS}{dt}$ is the surface recession rate (directly related to the surface mass loss rate) in m.s^{-1} .

Our results are summarized in Fig. 7, which shows the heliocentric and mean distances³ r_A and d_A (black and grey lines, respectively), for two particular asteroids. In addition, we have plotted the cumulative surface recession $\Delta S = \sum \frac{dS}{dt} \Delta t$, as a function of time, for $A = 0.05$ and $A = 0.50$ (solid and dashed red lines, respectively). For the first asteroid (top panel), we can recognize several crosses with the HZ (solid blue lines), at $t \approx 6700, 9700$ and 14000 years, where collisions with an EP could occur. In case there is a collision at ~ 1.0 au, this asteroid could lose between 1.5 and 6.5 km of its surface (according to the different values of the albedo A). The surface recession is moderate as the asteroid can collide no longer after the beginning of the integration. For the other asteroid (bottom panel), the first possible collision occurs at $t \approx 2.5 \times 10^6$ years where ΔS is between 90 and 700 km. In this case, it is very unlikely that this asteroid can deliver water initially located on its surface because its surface would become dry.

4.2. Atmospheric drag

Planetary atmospheric properties depend strongly on the stage of formation of the EP. Indeed, during the disk-embedded phase of a protoplanet, primordial atmospheres

³ these two quantities show how eccentric the orbit of the asteroid is when the solid grey and black lines do not overlap

are hot, dense structures which can extend to the proto-planet’s Hill radius (Stökl et al. 2016). Because none of the terrestrial planets in the current state of our solar system show remnants of such primordial atmospheres, they probably must vanish at some time right after the disk phase. In order to estimate the mass loss ΔM of a Ceres-like object due to thermal ablation (Podolak et al. 1988) caused by atmospheric drag, we proceed as follows.

1. we consider that the maximum mass loss accounts for a primordial atmosphere extended to one Hill radius. As suggested by (Ragossnig et al. 2017, in prep.), we consider atmospheric parameters (density and temperature) at 1 Myr in order to guarantee a quasi-stationary atmosphere. Furthermore, the typical lifespan of the inner disk is believed to be around 1 to 3 Myr (see Williams and Cieza 2011), which accounts for a regime where we assume a primordial atmosphere immediately after the disk phase, with maximum temperature and density. The body is then dropped from one Hill radius with an initial velocity such as the final impact velocity \bar{v}_i of the asteroid, after traveling through the atmosphere, fits with our results presented in Sec. 3.2. The variation of mass ΔM evaluated from one Hill radius to the EP’s radius define the maximum mass loss. Due to the low gravity of the Moon, we neglected any effect of atmospheric pressure. We thus assume no mass loss in this case.

2. Depending on the EP’s mass, the evolution of the primordial atmosphere can have different outcomes, as stated earlier. We thus consider that the minimum mass loss accounts for (1) either a present atmospheric model, as defined by the International Standard Atmosphere (ISA) in the case of the Earth⁴ or (2) no presence of atmosphere around the EP, in the case of Mars- and the Moon-sized objects. In this latter case, we assume no mass loss.

Figure 8 shows the mass loss ΔM of a Ceres-like body colliding with an Earth-type (bottom panel) or a Mars-type body (top panel) with different initial impact velocities \bar{v}_i . The black lines define the maximum mass loss due to the primordial atmosphere and the red line gives the minimum mass loss, for the Earth only, according to the ISA atmospheric model. As we can see, a Ceres-like asteroid entering the Hill radius of an Earth-like would lose a maximum of 15 – 85% of its initial mass, depending on its initial velocity. It is very unlikely that water can reach the EP’s surface in this

⁴ in this case, the atmospheric ISA values were extrapolated up to one Hill radius

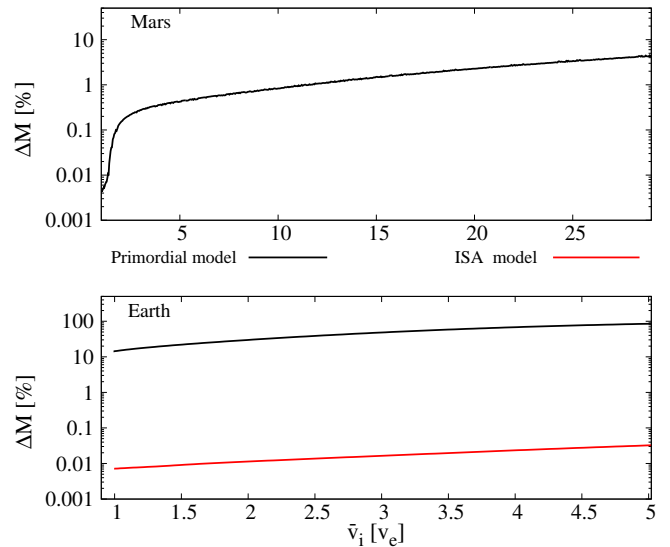


Figure 8. Mass variation ΔM of a Ceres-like under a primordial atmospheric pressure model (black line) for the Earth and Mars, or an atmospheric model according to the ISA (red line), for the Earth only.

case⁵. A primordial atmosphere of a Mars-like would cause a maximum loss of 5% for high impact velocities, allowing the asteroid to keep almost all of its initial water content. On a later stage of planetary formation, the atmospheric pressure according to the ISA parameters will have no effect on the asteroid’s mass as the minimum mass loss is always below 0.1%.

5. SUMMARY AND CONCLUSION

In this paper, we investigated the influence of the location of orbital resonances (SR and MMRs) on the water transport onto EPs (Earth-, Mars- and Moon-sized objects) orbiting inside the habitable zone (HZ). For given binary configurations, the gas giant semi-major axis was chosen such that an SR lies either in the HZ at ~ 1.0 au (causing high eccentric motion therein) or in the asteroid belt beyond the snow line at 2.7 au (and nearly circular motion in the HZ). We first showed that the frequency of asteroids reaching the HZ region (and even Mercury’s distances) is much higher when the SR is inside the asteroid belt due to overlaps with MMRs. As a consequence, this produces a higher number of impactors on the EP’s surface and therefore, a higher water transport. In addition, we showed that the presence of an SR and MMR inside the HZ could boost the water transport as the EPs can collide with more asteroids. This is apparently a positive mechanism for the water transport efficiency. However, our study shows clearly that dynamical results overestimate the water transport and need to be corrected by real

⁵ However, fragments can remain in the EP’s atmosphere

simulations of collisions that provide the water loss due to an impact. Indeed, we showed that collisions in the HZ can occur with high impact velocities causing significant water loss for the asteroid (up to 100%) when colliding at the EP's surface. The amount of water reaching the EP can be reduced by more than 50%.

During planetary formation, EPs also collide with each other and can transfer a fraction of their water content to each other. However, the merging approach generally used in simulations can overestimate the water content and mass of the surviving body resulting from the collision. SPH collision scenarios between embryo-sized objects have to be carried out in order to derive impact angles and velocity distributions, which will be the topic for a future work.

Even if water on the asteroid's surface may survive the collision, other mechanisms can significantly alter the wmf of asteroids, long before a collision. In this context, we were interested in ice sublimation, which can cause a severe recession of the asteroid's surface if they collide with an EP too long after the gas vanishes. Moreover, the primordial atmosphere of an EP can contribute up to 80% of an asteroid's mass loss due to high impact velocity.

It is very likely that an asteroids' surface can become dry even before colliding in the HZ. Even if a water layer can

resist, it might not survive the impact on the EP's surface. However, we cannot ignore that asteroids have indeed contributed to bring most of the water present on Earth's surface as the D/H ratio of chondrites asteroids matches with that of the Earth (Altwegg et al. 2015). Recently, Küppers et al. (2014) reported water emission from Ceres using *Herschel* observations. However, there are uncertainties on the location of the ice layer even if Formisano et al. (2016) showed that an ice layer located only a few centimeters under the surface can explain the rate of produced water molecules. A possibility would be that the water of such icy objects is located beneath the surface and therefore, protected from early sublimation. This will be the subject of a future study.

ACKNOWLEDGEMENTS

D.B, E.P.-L., T.I.M. and F.R. acknowledge the support of the Austrian Science Foundation (FWF) NFN project: Pathways to Habitability and related sub-projects S11608-N16 "Binary Star Systems and Habitability", S11603-N16 "Water transport" and S11604-N16 "Stars". D.B. and E.P.-L. also acknowledge the Vienna Scientific Cluster (VSC project 70320) for computational resources.

REFERENCES

- K. Altwegg, H. Balsiger, A. Bar-Nun, J. J. Berthelier, A. Bieler, P. Bochsler, C. Briosis, U. Calmonte, M. Combi, J. De Keyser, P. Eberhardt, B. Fiethe, S. Fuselier, S. Gasc, T. I. Gombosi, K. C. Hansen, M. Hässig, A. Jäckel, E. Kopp, A. Korth, L. LeRoy, U. Mall, B. Marty, O. Mousis, E. Neefs, T. Owen, H. Rème, M. Rubin, T. Sémon, C.-Y. Tzou, H. Waite, and P. Würz. 67P/Churyumov-Gerasimenko, a Jupiter family comet with a high D/H ratio. *Science*, 347(27):1261952, January 2015.
- D. Bancelin, E. Pilat-Lohinger, S. Ettl, T. I. Maindl, C. Schäfer, R. Speith, and R. Dvorak. Asteroid flux towards circumprimary habitable zones in binary star systems. I. Statistical overview. *A&A*, 581:A46, September 2015.
- D. Bancelin, E. Pilat-Lohinger, and A. Bazso. Asteroid flux towards circumprimary habitable zones in binary star systems. II. Dynamics. *A&A*, 591:A120, June 2016.
- Á. Bzszó, E. Pilat-Lohinger, S. Ettl, B. Funk, D. Bancelin, and G. Rau. Dynamics and habitability in circumstellar planetary systems of known binary stars. *MNRAS*, 466:1555–1566, April 2017.
- W. Benz and E. Asphaug. Impact simulations with fracture. I - Method and tests. *Icarus*, 107:98, January 1994.
- W. Benz and E. Asphaug. Simulations of brittle solids using smooth particle hydrodynamics. *Computer Physics Communications*, 87:253–265, May 1995.
- C. Burger. Equilibrium conditions of multi-material particle distributions in SPH simulations of colliding planetesimals in early planetary systems. *Master-Thesis, University of Vienna, Austria*, 2015.
- M. Formisano, M. C. De Sanctis, G. Magni, C. Federico, and M. T. Capria. Ceres water regime: surface temperature, water sublimation and transient exo(atmo)sphere. *MNRAS*, 455: 1892–1904, January 2016.
- R. Gomes, H. F. Levison, K. Tsiganis, and A. Morbidelli. Origin of the cataclysmic Late Heavy Bombardment period of the terrestrial planets. *Nature*, 435:466–469, May 2005.
- N. Haghighipour and S. N. Raymond. Habitable Planet Formation in Binary Planetary Systems. *ApJ*, 666:436–446, September 2007.
- Kenneth C. Hansen, K. Altwegg, J.-J. Berthelier, A. Bieler, N. Biver, D. Bockelée-Morvan, U. Calmonte, F. Capaccioni, M. R. Combi, J. De Keyser, B. Fiethe, N. Fougere, S. A. Fuselier, S. Gasc, T. I. Gombosi, Z. Huang, L. Le Roy, S. Lee, H. Nilsson, M. Rubin, Y. Shou, C. Snodgrass, V. Tennishev, G. Toth, C.-Y. Tzou, C. Simon Wedlund, and the ROSINA team. Evolution of water production of 67p/churyumov-gerasimenko: An empirical model and a multi-instrument study. *Monthly Notices of the Royal Astronomical Society*, 2016.

- M. J. Holman and P. A. Wiegert. Long-Term Stability of Planets in Binary Systems. *AJ*, 117:621–628, January 1999.
- D. Jewitt. The Active Asteroids. *AJ*, 143:66, March 2012.
- R. K. Kopparapu, R. Ramirez, J. F. Kasting, V. Eymet, T. D. Robinson, S. Mahadevan, R. C. Terrien, S. Domagal-Goldman, V. Meadows, and R. Deshpande. Habitable Zones around Main-sequence Stars: New Estimates. *ApJ*, 765:131, March 2013.
- M. Küppers, L. O’Rourke, D. Bockelée-Morvan, V. Zakharov, S. Lee, P. von Allmen, B. Carry, D. Teyssier, A. Marston, T. Müller, J. Crovisier, M. A. Barucci, and R. Moreno. Localized sources of water vapour on the dwarf planet (1)Ceres. *Nature*, 505:525–527, January 2014.
- C. Lécuyer, P. Grandjean, J.-A. Barrat, J. Nolvak, C. Emig, F. Paris, and M. Robardet. $\delta^{18}\text{O}$ and REE contents of phosphatic brachiopods: a comparison between modern and lower Paleozoic populations. *Geochim. Cosmochim. Acta*, 62: 2429–2436, July 1998.
- Z. M. Leinhardt and S. T. Stewart. Collisions between Gravity-dominated Bodies. I. Outcome Regimes and Scaling Laws. *ApJ*, 745:79, January 2012.
- T. I. Maindl, C. Schäfer, R. Speith, Á. Süli, E. Forgács-Dajka, and R. Dvorak. SPH-based simulation of multi-material asteroid collisions. *Astronomische Nachrichten*, 334(9), 2013. ISSN 1521-3994.
- T. I. Maindl, R. Dvorak, C. Schäfer, and R. Speith. Fragmentation of colliding planetesimals with water content. In *Complex Planetary Systems, Proceedings of the International Astronomical Union*, volume 310 of *IAU Symposium*, pages 138–141, July 2014.
- A. Morbidelli, J. Chambers, J. I. Lunine, J. M. Petit, F. Robert, G. B. Valsecchi, and K. E. Cyr. Source regions and time scales for the delivery of water to Earth. *Meteoritics and Planetary Science*, 35:1309–1320, November 2000.
- L. R. Mudryk and Y. Wu. Resonance Overlap Is Responsible for Ejecting Planets in Binary Systems. *ApJ*, 639:423–431, March 2006.
- D. P. O’Brien, K. J. Walsh, A. Morbidelli, S. N. Raymond, and A. M. Mandell. Water delivery and giant impacts in the ‘Grand Tack’ scenario. *Icarus*, 239:74–84, September 2014.
- T. Owen and A. Bar-Nun. Comets, Impacts, and Atmospheres. *Icarus*, 116:215–226, 1995.
- E. Pilat-Lohinger. The role of dynamics on the habitability of an Earth-like planet. *International Journal of Astrobiology*, 14: 145–152, April 2015.
- E. Pilat-Lohinger and R. Dvorak. Stability of S-type Orbits in Binaries. *Celestial Mechanics and Dynamical Astronomy*, 82: 143–153, February 2002.
- E. Pilat-Lohinger, P. Robutel, Á. Süli, and F. Freistetter. On the stability of Earth-like planets in multi-planet systems. *Celestial Mechanics and Dynamical Astronomy*, 102:83–95, September 2008a.
- E. Pilat-Lohinger, Á. Süli, P. Robutel, and F. Freistetter. The Influence of Giant Planets Near a Mean Motion Resonance on Earth-like Planets in the Habitable Zone of Sun-like Stars. *ApJ*, 681:1639–1645, July 2008b.
- E. Pilat-Lohinger, A. Bazsó, and B. Funk. A Quick Method to Identify Secular Resonances in Multi-planet Systems with a Binary Companion. *AJ*, 152:139, November 2016.
- M. Podolak, J. B. Pollack, and R. T. Reynolds. Interactions of planetesimals with protoplanetary atmospheres. *Icarus*, 73: 163–179, January 1988.
- F. Ragossnig, A. Stökl, E. A. Dorfi, D. Steiner, and M. Güdel. Interaction of in-falling solid bodies with the primordial disk embedded planetary atmosphere. *in prep.*, 2017.
- C. Schäfer, R. Speith, and W. Kley. Collisions between equal-sized ice grain agglomerates. *A&A*, 470:733–739, August 2007.
- C. Schäfer, S. Riecker, T. I. Maindl, R. Speith, S. Scherrer, and W. Kley. A smooth particle hydrodynamics code to model collisions between solid, self-gravitating objects. *A&A*, 590: A19, May 2016.
- D. I. Shestopalov and L. F. Golubeva. Bond Albedo of Asteroids from Polarimetric Data. In *Lunar and Planetary Science Conference*, volume 42 of *Lunar and Planetary Science Conference*, page 1028, March 2011.
- G. Sitarski. Approaches of the Parabolic Comets to the Outer Planets. *Acta Astron.*, 18:171, 1968.
- A. Stökl, E. A. Dorfi, C. P. Johnstone, and H. Lammer. Dynamical Accretion of Primordial Atmospheres around Planets with Masses between 0.1 and 5 M_{\oplus} in the Habitable Zone. *ApJ*, 825: 86, July 2016.
- P. Thebault and N. Haghighipour. Planet formation in Binaries. *ArXiv e-prints*, June 2014.
- J. H. Tillotson. Metallic equations of state for hypervelocity impact. Technical Report General Atomic Report GA-3216, General Dynamics, San Diego, CA, 1962.
- K. Tsiganis, R. Gomes, A. Morbidelli, and H. F. Levison. Origin of the orbital architecture of the giant planets of the Solar System. *Nature*, 435:459–461, May 2005.
- K. J. Walsh, A. Morbidelli, S. N. Raymond, D. P. O’Brien, and A. M. Mandell. A low mass for Mars from Jupiter’s early gas-driven migration. *Nature*, 475:206–209, July 2011.
- J. P. Williams and L. A. Cieza. Protoplanetary Disks and Their Evolution. *ARA&A*, 49:67–117, September 2011.